Negative refraction in quasicrystalline multilayered metamaterials

Lorenzo Morini[a], Yoann Eyzat[b], Massimiliano Gei[a,*]

[a] School of Engineering, Cardiff University, The Parade, Cardiff CF24 3AA, Wales, UK
[b] École Nationale Supérieure de Mécanique et d'Aérotechnique (ISAE-ENSMA), 1 avenue Clément d'Ader, F-86961 Futuroscope-Chasseneuil Cedex, France

ARTICLE INFO

Article history:
Received 26 July 2018
Revised 12 October 2018
Accepted 16 October 2018
Available online 19 October 2018

Keywords:
Fibonacci laminates
Kohmoto's invariant
Quasiperiodic structure
Poynting vector
Composite material
Elastic wave

ABSTRACT

Inspired by some recent results in elastodynamics of layered composites, we address here the problem of an antiplane elastic wave obliquely incident at the interface between a substrate and a periodic laminate with a quasicrystalline structure (generated by the Fibonacci substitution rule). The angles of refraction of the transmitted modes are computed by combining the transfer matrix method with the normal mode decomposition and evaluating the direction of the average Poynting vector. It is shown that, with respect to a periodic classical bilayer, on the one hand, beyond a certain frequency threshold, high order Fibonacci laminates can provide negative refraction for a wider range of angles of incidence, on the other, they allow negative wave refraction at lower frequencies. The outcome strongly relies on the Floquet–Bloch dynamic analysis of this class of laminates that is performed thoroughly. It is revealed that the corresponding spectra have a self-similar character linked to the specialisation of the Kohmoto's invariant, a function of the frequency that was recently studied by the authors for periodic one-dimensional quasicrystalline-generated waveguides. This function is able to explain two types of scaling occurring in dispersion diagrams. The attained results represent an important advancement towards the realisation of multilayered quasicrystalline metamaterials with the aim to control negatively refracted elastic waves.

1. Introduction

In the last fifty years, several authors have shown that periodic multilayers can significantly affect the propagation of elastic waves (Hegemier and Nayfeh, 1973; Nemat-Nasser, 1972; Nemat-Nasser et al., 1975; Rudykh and Boyce, 2014; Shmuel and Band, 2016; Sun et al., 1968). The promising properties revealed by these studies have inspired an extensive research activity concerning the design of phononic composites based on both continuous and discrete (lattice-based) periodic media. Several applications have been proposed for these structures including wave focussing (Guenneau et al., 2007; Yang et al., 2004), frequency filtering (Khelif et al., 2003; Wang et al., 2004; Wu et al., 2009), negative refraction (Chen et al., 2017; Morvan et al., 2010; Zhang and Liu, 2004; Zhu et al., 2014), mode conversion (Vines et al., 1999), beam splitting (Roberts et al., 1983, 1985) and beam steering (Romanoni et al., 2009). The related literature is extremely vast and diversified and

* Corresponding author.
E-mail addresses: morinil@cardiff.ac.uk (L. Morini), geim@cardiff.ac.uk (M. Gei).

https://doi.org/10.1016/j.jmps.2018.10.016

the most relevant results are summarized in some excellent review papers such as Hussein et al. (2014); Lee et al. (2012); Pennec et al. (2010) and Srivastava (2015).

Recently, Nemat-Nasser (2015a,b); Srivastava (2016); Willis (2016) and Srivastava and Willis (2017) investigated a specific elastic problem within this field: the oblique incidence of an antiplane shear wave at the interface between a substrate and a periodic bilayer laminate. These studies suggested that, when the layering direction is perpendicular to the interface, it is possible to use a laminate to induce negative refraction, a phenomenon that is generally observed when elastic waves impinge tailored-designed micro-architected interfaces (Brun et al., 2010; Jones et al., 2011; Sukhovich et al., 2008). More in detail, the results provided by Willis (2016) show that, under some hypotheses, by assuming a determinate frequency for the incident wave, the transmitted signal consists of coexisting positively and negatively refracted waves (beam splitting). In order to avoid this splitting and to achieve single negatively refracted modes, it is necessary to couple the incident wave with the laminate modes in the second Brillouin zone (Srivastava, 2016). Depending on the characteristics of the elastic substrate, a minimum wave frequency and a threshold angle of incidence can be determined to reach the second Brillouin zone.

In this paper, with the aim of deepening the understanding of negative refraction in elastic laminates, we study the same problem of the transmission of an antiplane wave at a substrate-laminate interface by considering a class of two-phase periodic layered composites whose unit cells, each of which is associated with an integer index (also called the 'order' of the sequence), are generated according to the Fibonacci substitution rule (*Fibonacci laminates*). The reason is based on a recent research on wave propagation of one-dimensional structured two-phase quasicrystalline rods (Morini and Gei, 2018) which has revealed intriguing dynamic properties when the location of phases are assigned following that law. More in detail, in the present context the Fibonacci rule generates a particular subset of quasiperiodic laminates, classified as *quasicrystalline* (Poddubny and Ivchenko, 2010). Morini and Gei (2018) have shown that the dynamic spectra of the analogous family of one-dimensional rods are governed by an invariant function, the Kohmoto's invariant, that is independent of the order and depends only on the circular frequency. The Kohmoto's invariant can explain two types of scaling featuring the general layout of stop and pass bands for the family of rods, i.e. a *local* scaling and a *global* one, and the existence of ultrawide band gaps that are common to all orders of the sequence.

In the first part of the article, by applying the transfer matrix method (Thomson, 1950), we derive the Floquet–Bloch dispersion relation for this new class of layered composites. The computed dynamic spectra are characterised by a self-similar layout of *transition zones*, which are ranges of frequency where the number of propagating modes in the laminate depends on the transverse wave number; their location as functions of the frequency is similar to that of stop bands for the one-dimensional quasicrystalline structured rods presented by Morini and Gei (2018), therefore they display scaling laws that can be studied with a specialisation of the Kohmoto's invariant.

The transmitted and reflected waves at the interface between elastic half space and the introduced class of laminates are then analysed by means of the normal mode decomposition (Srivastava and Willis, 2017). The Poynting vector and group velocity for waves propagating through the laminate are evaluated and exploited to estimate the corresponding angles of refraction. The attained results show that, concerning the possibility of obtain negative refraction, Fibonacci laminates possess some properties that are not available in standard periodic two-phase materials. In particular, with respect to the already investigated bilayer laminate:

- beyond a certain frequency threshold, high-order Fibonacci laminates admit negative refraction for a wider range of angles of incidence; in some cases, a negative refraction mode is attainable for any angle of incidence. The trend increases monotonically at increasing order of the sequence;
- by assuming the same angle of incidence for the impinging wave, using the proposed quasicrystalline composite it is possible to produce a single transmitted negatively refracted wave at lower frequencies without the need to change the materials composing the laminae as required for a simple bilayer (Srivastava, 2016). This is achievable as propagating modes in the second Brillouin zone become available at lower frequencies.

A further interesting feature is that the position of transition zones varying the order of the sequence is governed in an approximate way by two types of scaling, a local one and a global one. The latter may be used as a predicting tool to select the most suitable laminate of the family that, in combination to a given substrate, may ensure the availability of a single negatively refracted transmitted mode.

The proposed methodology and the results obtained in this paper, though restricted to a particular choice of the materials composing the two phases, suggest that Fibonacci –and, in general, quasicrystalline–laminates may be profitably employed to conceive elastic metamaterial devices with the aim to realise flat lenses or focus waves in a circumscribed area to harvest mechanical energy.

2. Floquet–Bloch waves in periodic quasicrystalline laminates

In this Section, we define the class of two-dimensional, two-phase laminates whose elementary cell is generated according to the Fibonacci substitution rule. Preliminary results concerning propagation of Floquet–Bloch waves in this type of layered media are reported.

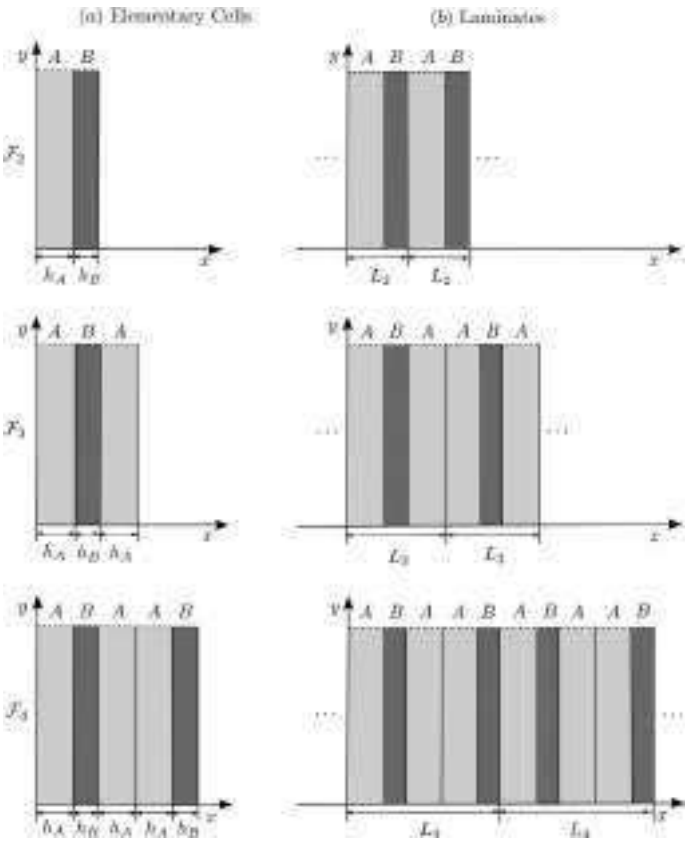

Fig. 1. a) Elementary cells generated by Fibonacci sequences $\mathcal{F}_2$, $\mathcal{F}_3$ and $\mathcal{F}_4$; b) two-dimensional laminates assembled according to $\mathcal{F}_2$, $\mathcal{F}_3$ and $\mathcal{F}_4$. Axis z is the out-of-plane direction.

2.1. Fibonacci laminates: governing equations and dispersion relations

Let us introduce a class of two-dimensional, two-phase quasicrystalline laminates with layering direction parallel to the axis y (see Fig. 1). Each of its elements is composed of a repeated elementary cell where the two basic components, A and B, are arranged in series according to the standard Fibonacci sequence, which is based on the following substitution rule:

$$A \to AB, \quad B \to A. \tag{1}$$

Repetition of the fundamental cells assures global periodicity along axis x and the possibility of applying the Floquet–Bloch technique in order to study harmonic wave propagation in these systems (Gei, 2010).

The substitutive relation (1) implies that the finite Fibonacci sequence of the i−th order ($i = 0, 1, 2, \dots$), here denoted by $\mathcal{F}_i$, obeys the recursive rule

$$\mathcal{F}_i = \mathcal{F}_{i-1}\mathcal{F}_{i-2}, \tag{2}$$

where the initial conditions are $\mathcal{F}_0 = B$ and $\mathcal{F}_1 = A$. The total number of elements of $\mathcal{F}_i$ corresponds to the Fibonacci number n_i, namely

$$n_i = n_{i-1} + n_{i-2} \qquad (i = 2, 3, 4, \dots), \tag{3}$$

with $n_0 = n_1 = 1$; moreover, $\lim_{i\to\infty} n_{i+1}/n_i = \sigma_g$, where $\sigma_g = (1 + \sqrt{5})/2$ is the so-called *golden mean* ratio.

For each phase, shear modulus μ_X, mass density ρ_X and thickness h_X (here and henceforth, $X \in \{A, B\}$) are defined, and the j-th layer composing the elementary cell occupies the domain $x_j < x < x_j + h_X \equiv x_{j+1}$. Along x, the total length of cell $\mathcal{F}_i$ is given by $L_i = n_i^{(A)} h_A + n_i^{(B)} h_B$, where $n_i^{(A)}$ and $n_i^{(B)}$ are the number of elements A and B contained in the cell, respectively.

We now assume that an antiplane shear wave propagates in the laminate just described. The only non-zero component of the displacement is taken to be $u_z(x, y, t)$, and within the j-th phase of the elementary cell it satisfies the wave equation

$$\frac{\partial^2 u_z}{\partial x^2} + \frac{\partial^2 u_z}{\partial y^2} = \frac{1}{c_X^2}\frac{\partial^2 u_z}{\partial t^2}, \tag{4}$$

where $c_X = \sqrt{\mu_X/\rho_X}$ denotes the shear wave speed in the relevant materials. The solution to Eq. (4) has the form

$$u_z(x, y, t) = w(x)\ \exp[\mathrm{i}(\omega t - K_x x - K_y y)], \tag{5}$$

where ω is the circular frequency and the function $w(x)$ is periodic with period L_i. The antiplane displacement gives rise to the non-vanishing stress components $\sigma_{xz}(x, y, t)$ and $\sigma_{yz}(x, y, t)$. Functions $u_z(x, y, t)$ and $\sigma_{xz}(x, y, t)$ are continuous across all the interfaces and therefore, within the lamina j, they can be expressed as

$$\begin{pmatrix} \sigma_{xz}(x) \\ u_z(x) \end{pmatrix} = \boldsymbol{M}_X(x - x_j) \begin{pmatrix} \sigma_{xz}(x_j) \\ u_z(x_j) \end{pmatrix}, \tag{6}$$

where the dependency on y and t has been dropped and the *transfer* (or *transmission*) matrix $\boldsymbol{M}_X$ assumes the form

$$\boldsymbol{M}_X(\xi) = \begin{bmatrix} \cos(q_X\xi) & -\mu_X q_X \sin(q_X\xi) \\ \sin(q_X\xi)/(\mu_X q_X) & \cos(q_X\xi) \end{bmatrix}, \tag{7}$$

with $q_X = [(\omega/c_X)^2 - K_y^2]^{1/2}$. Therefore, by applying the Floquet–Bloch conditions on the boundary of the elementary cell, we have

$$\begin{pmatrix} \sigma_{xz}(L_i) \\ u_z(L_i) \end{pmatrix} = \boldsymbol{M}_i \begin{pmatrix} \sigma_{xz}(0) \\ u_z(0) \end{pmatrix} = \exp(-\mathrm{i}K_x L_i) \begin{pmatrix} \sigma_{xz}(0) \\ u_z(0) \end{pmatrix}, \tag{8}$$

where $\boldsymbol{M}_i$ is the global transmission matrix of the cell associated with the sequence $\mathcal{F}_i$:

$$\boldsymbol{M}_i = \prod_{p=1}^{n_i} [\boldsymbol{M}_X(h_X)]_p. \tag{9}$$

Matrix $\boldsymbol{M}_i$ is unimodular, i.e. $\det \boldsymbol{M}_i = 1$, and follows the recursion rule $\boldsymbol{M}_{i+1} = \boldsymbol{M}_{i-1}\boldsymbol{M}_i$, with $\boldsymbol{M}_0 = \boldsymbol{M}_B$ and $\boldsymbol{M}_1 = \boldsymbol{M}_A$. Using the former property and Eq. (8), the following dispersion relation can be easily derived,

$$\cos(K_x L_i) = \frac{1}{2}\mathrm{tr}\boldsymbol{M}_i. \tag{10}$$

By observing Eq. (10), we deduce that all the information concerning wave propagation in a generic laminate is contained in the trace of the corresponding transmission matrix.

2.2. Trace recursive relations and Kohmoto's invariant

Let us now note that the transfer matrix (7) and the dispersion relation (10) are similar to those introduced by Morini and Gei (2018) to study axial wave propagation in Fibonacci quasicrystalline-structured rods. In analogy with the approach developed in that paper, we can now use the unimodularity property of $\boldsymbol{M}_i$ ($\det \boldsymbol{M}_i = 1$) to derive a recursive relation for the traces $\mathrm{tr}\boldsymbol{M}_i$. Introducing the notation $t_i = \mathrm{tr}\boldsymbol{M}_i$, for given ω and K_y, the equation

$$t_{i+1} = t_{i-1}t_i - t_{i-2} \qquad (i = 2, 3, 4, \ldots) \tag{11}$$

is valid. Relationship (11) can be easily verified by specialising the expressions for the traces of unimodular 2×2 transfer matrices of generalised Fibonacci chains derived by Kolar and Ali (1989) and Kolar and Nori (1990) in terms of Chebyshev polynomials of first and second kind. By means of the expression (11), it can be also demonstrated (see Morini and Gei, 2018 for more details) that the Kohmoto's invariant

$$\begin{aligned} I(\omega, K_y) &= t_{i+2}^2 + t_{i+1}^2 + t_i^2 - t_{i+2}t_{i+1}t_i - 4 \\ &= \frac{(\mu_A^2 q_A^2(\omega, K_y) - \mu_B^2 q_B^2(\omega, K_y))^2}{\mu_A^2 q_A^2(\omega, K_y)\mu_B^2 q_B^2(\omega, K_y)} \sin^2\left[h_A q_A(\omega, K_y)\right] \sin^2\left[h_B q_B(\omega, K_y)\right] \end{aligned} \tag{12}$$

is constant for any arbitrary triad of consecutive traces (t_{i+2}, t_{i+1}, t_i). This means that the value of $I(\omega, K_y)$ is independent of the order i of the fundamental cell $\mathcal{F}_i$. This function is used here to describe the self-similar properties and scaling of the dynamic spectra of Fibonacci laminates. In particular, a great relevance is assumed by the specialisation $I_0(\omega) = I(\omega, 0)$, given by

$$I_0(\omega) = \frac{(\mu_A\rho_A - \mu_B\rho_B)^2}{\mu_A\rho_A\mu_B\rho_B} \sin^2\left(\frac{h_A\omega}{c_A}\right) \sin^2\left(\frac{h_B\omega}{c_B}\right), \tag{13}$$

which is analogous to that derived by Morini and Gei (2018) in their problem. The significance of case $K_y = 0$ will be clarified in Section 2.3 where the notion of transition zone will be introduced.

As far as scaling is concerned, on the basis of the recursive relation (11), Morini and Gei (2018) studied the variation of the triad of consecutive traces $(t_{i+2}, t_{i+1}, t_i) = (\tilde{x}_i, \tilde{y}_i, \tilde{z}_i)$ from one cell to another as the evolution of the nonlinear discrete map

$$\mathcal{T}(\tilde{x}_i, \tilde{y}_i, \tilde{z}_i) = (\tilde{x}_{i+1}, \tilde{y}_{i+1}, \tilde{z}_{i+1}) = (\tilde{x}_i\tilde{y}_i - \tilde{z}_i,\ \tilde{x}_i,\ \tilde{y}_i). \tag{14}$$

For any given value of the frequency, the points obtained by iterating the map (14) are all confined on the three-dimensional Kohmoto's surface whose equation in the continuous three-dimensional space $O\tilde{x}\tilde{y}\tilde{z}$ is $\tilde{x}^2+\tilde{y}^2+\tilde{z}^2-\tilde{x}\tilde{y}\tilde{z}-4=I_0(2\pi f)$ (we focus here on the case $K_y=0$, relevant for our study). Each Kohmoto's surface possesses six saddle points connected through a closed (periodic) orbit generated by a six-cycle transformation obtained by applying six times map (14). The 'discrete' trajectory traced by the point $(t_{i+2},t_{i+1},t_i)=(\tilde{x}_i,\tilde{y}_i,\tilde{z}_i)$ at increasing index on the Kohmoto's surface is then studied as a small perturbation of the periodic orbit with map (14) linearised about the six saddle points. The derived linearised transformation has one eigenvalue equal to one and an additional pair of them given by

$$\kappa_0^{\pm}(f)=\frac{1}{4}\left(\sqrt{4+(4+I_0(2\pi f))^2}\pm(4+I_0(2\pi f))\right)^2. \tag{15}$$

In both Morini and Gei (2018) and Gei (2010) it is shown that the quantity $\kappa_0^+(f)$ ($\sqrt{\kappa_0^+(f)}$) governs the local scaling occurring between localised ranges of the spectrum of cell $\mathcal{F}_i$ and that of $\mathcal{F}_{i+6}$ ($\mathcal{F}_{i+3}$). In particular, in frequency ranges where the local scaling is valid, a pass band, say $\{f_{i+6}^B-f_{i+6}^A\}$, in the diagram of cell $\mathcal{F}_{i+6}$ centred at a given value of the frequency f^* is related to the pass band $\{f_i^B-f_i^A\}$ in the diagram of cell $\mathcal{F}_i$ centred almost about the same value of f^* by the following scaling law

$$f_{i+6}^B-f_{i+6}^A\approx\frac{f_i^B-f_i^A}{\kappa}, \tag{16}$$

where $\kappa=\kappa_0^+(f^*)$. Similarly, with $\lambda=\sqrt{\kappa}$, it is

$$f_{i+3}^B-f_{i+3}^A\approx\frac{f_i^B-f_i^A}{\lambda}. \tag{17}$$

2.3. Dispersion curves and transition zones

The dispersion relation (10) is valid for generic complex values of ω and K_y. On the basis of this equation, we can easily deduce that K_x is real when $\mathrm{tr}\boldsymbol{M}_i\le 2$, and purely imaginary when $\mathrm{tr}\boldsymbol{M}_i>2$ (no complex values of K_x are found for antiplane waves propagating in purely elastic laminates) If K_x is a real solution to (10), then $\pm(K_x+2r\pi/L_i)$ ($r\in\mathbb{N}$) is also a solution.

For a real and positive circular frequency, a wave propagates along axis y for real and positive values of K_y, whilst it is evanescent if the same quantity is purely imaginary. We now show that for Fibonacci laminates of any order, there is a real and positive value $\bar{K}_y$ such that K_x is purely imaginary and the corresponding wave is propagating along the axis y if $K_y>\bar{K}_y$, but is evanescent along x. For this purpose, in Fig. 2 the real and imaginary parts of the normalized wave vector component K_xL_i are plotted against real values of K_yL_i for laminates $\mathcal{F}_2$ to $\mathcal{F}_5$. Following Nemat-Nasser (2015a), we assume throughout the paper that the materials of phases A and B are polymethyl–methacrylate (PMMA) and steel, respectively, therefore the relevant parameters are $\mu_A=3$ GPa, $\mu_B=80$ GPa, $\rho_A=1180$ kg/m^3, $\rho_B=8000$ kg/m^3, whereas the thicknesses of the two layers are $h_A=3$ mm and $h_B=1.3$ mm. A fixed value of the frequency $f=\omega/(2\pi)=220$ kHz was selected, and only purely real and positive values for K_y are taken into account as the interest lies here on propagating signals. $\mathrm{Re}(K_xL_i)$ has been restricted to the first Brillouin zone, namely $0<\mathrm{Re}(K_xL_i)<\pi$, but the analysis can be extended to the subsequent zones. By observing the plots in Fig. 2, we note that the normalized limit values are $\bar{K}_yL_2\approx 2.21$, $\bar{K}_yL_3\approx 5.24$, $\bar{K}_yL_4\approx 8.22$, $\bar{K}_yL_5\approx 9.25$ for $\mathcal{F}_2$, $\mathcal{F}_3$, $\mathcal{F}_4$ and $\mathcal{F}_5$, respectively. The detection of those values is in perfect agreement with the results obtained by Srivastava (2016) for two-phase periodic laminates, whose fundamental cell corresponds to $\mathcal{F}_2$ in our work. Numerical computations demonstrate that $\bar{K}_y$ depends upon the frequency under consideration and increases with f.

Fig. 2 also shows that below $\bar{K}_y$, there can be several real K_y solutions for a *given real* K_x (and also more than one real K_y's for a given imaginary K_x). At fixed frequency, the number of such real K_y solutions tends to increase with the generation index i of the composite. For instance, in the case here illustrated ($f=220$ kHz), we have one real K_y for $\mathcal{F}_2$, two for $\mathcal{F}_3$, three for $\mathcal{F}_4$ and five for cells generated by $\mathcal{F}_5$. This is also clearly illustrated in Figs. 3, 4 and 5, where the iso-frequency contour lines for real pairs $(K_xL_i,\ K_yL_i)$ in the first Brillouin zone are reported for cells $\mathcal{F}_2$, $\mathcal{F}_3$ and $\mathcal{F}_4$, respectively, and by observing the plotted curves, we can note that at rising frequencies, the number of solutions K_y corresponding to any given K_x increases, as well. Henceforth, the number of real solutions K_y corresponding to a given real value of K_x at frequency f in an arbitrary periodic cell $\mathcal{F}_i$ will be denoted by N_i^f.

Let us focus our attention now on dispersion curves corresponding to $f=270$ kHz in Fig. 3 (blue dashed lines). We note that in the range $2.15\le K_xL_2\le\pi$ there are two real K_yL_2 (corresponding to two propagating modes, i.e. $N_2^f=2$) while for $0\le K_xL_2<2.15$ only one real K_yL_2 is found (one single propagating mode, $N_2^f=1$). According to this property, $f=270$ kHz belongs to the second *transition zone* of cell $\mathcal{F}_2$. A *transition zone* is a frequency range in which N_i^f depends on the value of K_xL_i. The t-th transition zone is that where N_i^f switches from $t-1$ to t. For $\mathcal{F}_2$, the first transition zone is[1] $0<f<93$ kHz, the second one is $262<f<296$ kHz, and the third one $522<f<546$ kHz. For $\mathcal{F}_3$, the first, second and third transition zone correspond to ranges $0<f<63$ kHz, $132<f<161$ kHz and $264<f<282$ kHz, respectively. It is worth to remark that a limit of the transition zone corresponds to a frequency where a real solution branch K_y 'emerges' from $K_y=0$ at either $K_xL_i=0$ or

[1] Values of frequencies are rounded to the unit.

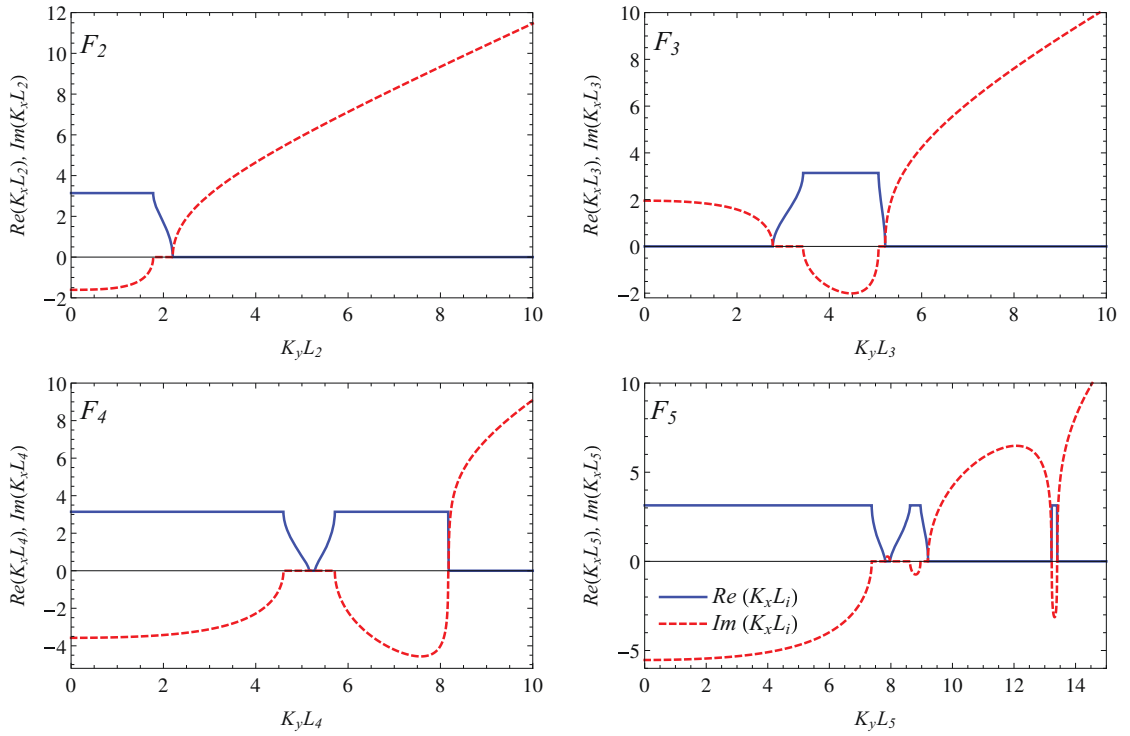

Fig. 2. Real (solid lines) and imaginary (dashed lines) parts of K_xL_i plotted against K_yL_i for Fibonacci laminates $\mathcal{F}_2$ to $\mathcal{F}_5$ at frequency $f = 220$ kHz. All values of K_y assumed in the calculations are real.

$K_xL_i = \pi$. This justifies the introduction of the invariant function (13) that will be used to study the self-similar properties of transition zones reported in red in the diagram of Fig. 11 for laminates $\mathcal{F}_2$–$\mathcal{F}_6$.

The modes illustrated in Figs. 3, 4 and 5 represent waves propagating along both x and y directions at a determinate frequency in Fibonacci laminates. Fig. 6 shows that at a given frequency, any real value of K_xL_i is associated with an infinite number of purely imaginary K_y solutions of the dispersion relation (10). These imaginary solutions correspond to an infinite number of waves travelling along x, but decaying exponentially along y (evanescent waves).

In (Willis, 2016), shear waves in the bilayer $\mathcal{F}_2$ are studied, and plots similar to those sketched in Fig. 3 are provided. For this unit cell, when there are two real solutions of K_y associated with the same K_x, the branch of the dispersion relation corresponding to the lower K_y has negative $x-$component of the group velocity. The analysis of the wave energy flux and Poynting vector reported by Srivastava (2016) shows that the achievement of negative group velocity components along axis x is crucial in order to observe negative refraction of elastic waves at the interface between a substrate and a laminate. For this reason, further in the paper we will study the group velocity of shear waves transmitted at the interface between substrates and quasicrystalline laminates, as for example those associated with the dispersion relations in Figs. 3, 4 and 5. In particular, we will investigate the transmission through the interface of propagating modes characterised by wave vector component K_xL_i belonging to the second Brillouin zone. The reported numerical results will show that this property allows us to use the Fibonacci laminates to obtain pure negative wave refraction at lower frequencies with respect to the case of standard two-phase periodic laminates.

3. Wave transmission and negative refraction

The methods to investigate transmission across and reflection at the interface between an elastic substrate and a quasicrystalline laminate of shear waves are now developed. Negative refraction is revealed under appropriate conditions and some specific filtering properties of these materials are compared with those of periodic 1-D phononic structures studied by Willis (2016) and Srivastava (2016).

3.1. Normal mode decomposition

Let us consider the problem of an elastic substrate with shear modulus μ_0 and mass density ρ_0 occupying the half-space $y < 0$ and bonded to a Fibonacci laminate with layering direction parallel to the axis y and occupying the region $y > 0$ (see Fig. 7). An antiplane wave is incident at the interface $y = 0$ from the homogeneous substrate with the incident angle θ. This

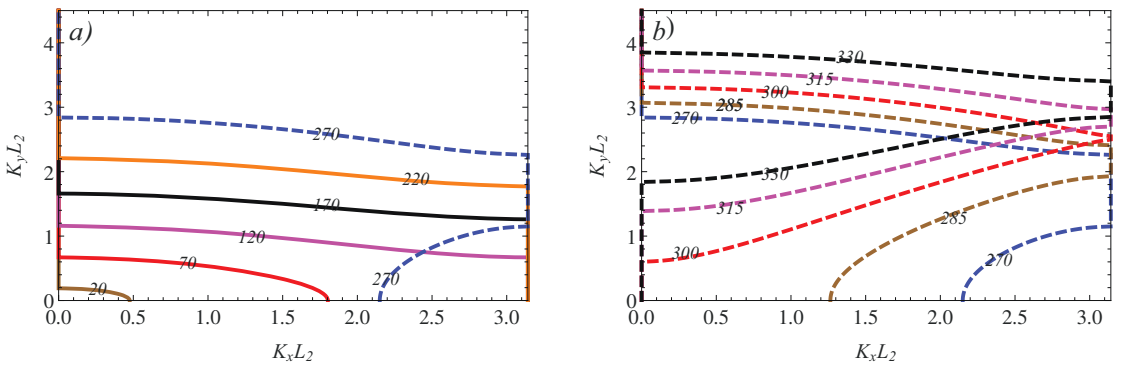

Fig. 3. Iso-frequency contours for real K_xL_2 and K_yL_2 for the laminate $\mathcal{F}_2$: a) frequency range $f = 0 - 270$ kHz; b) frequency range $f = 270 - 330$ kHz. Frequency values in kHz are reported onto the pertinent lines. Note that this case corresponds to that investigated by Willis (2016) and Srivastava (2016).

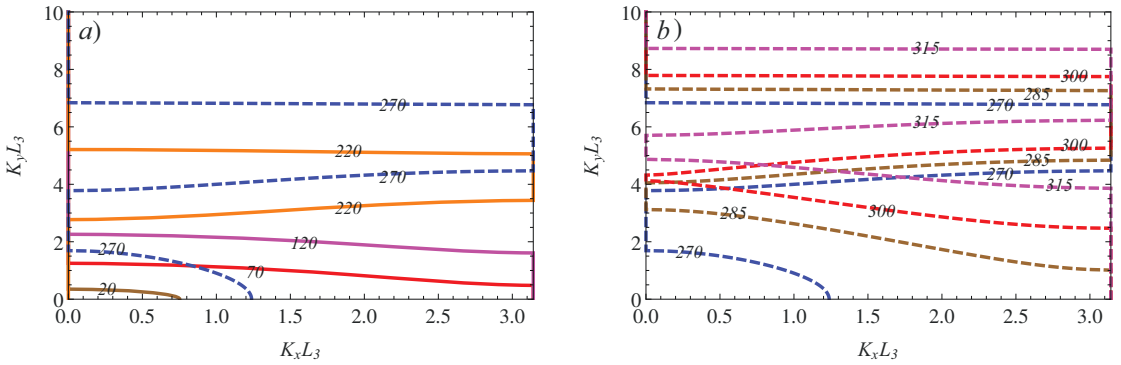

Fig. 4. Iso-frequency contours for real K_xL_3 and K_yL_3 for the laminate $\mathcal{F}_3$: a) frequency range $f = 0 - 270$ kHz; b) frequency range $f = 270 - 330$ kHz. Frequency values in kHz are reported onto the pertinent lines.

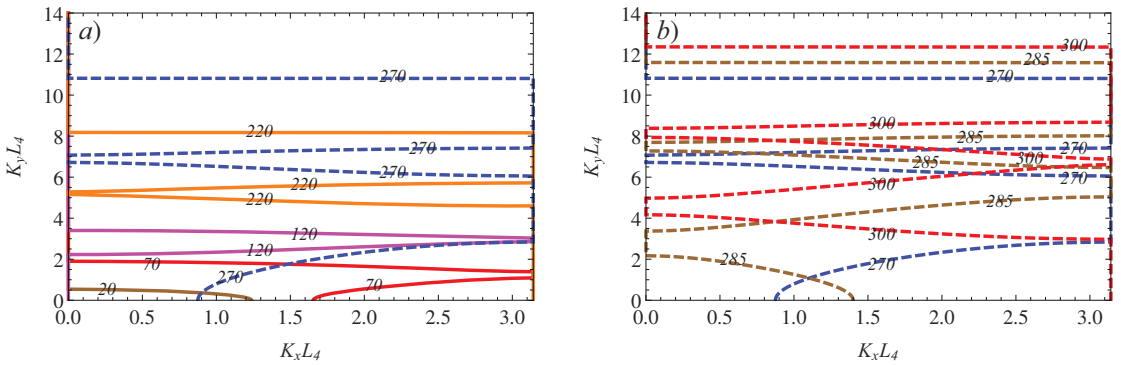

Fig. 5. Iso-frequency contours for real K_xL_4 and K_yL_4 for the laminate $\mathcal{F}_4$: a) frequency range $f = 0 - 270$ kHz; b) frequency range $f = 270 - 330$ kHz. Frequency values in kHz are reported onto the pertinent lines.

wave generates an infinite number of both transmitted and reflected modes. A finite number of these are propagating waves whereas the remaining are evanescent waves. We now introduce the following expressions for the incident, transmitted, and reflected fields, respectively:

$$u_z^{\text{inc}} = A\ \exp[\mathrm{i}(\omega t - K_0 x\cos\theta - K_0 y\sin\theta)], \tag{18}$$

$$u_z^{\text{trans}} = \sum_{\ell=0}^{\infty} T_\ell w_\ell(x)\ \exp\left[\mathrm{i}\left(\omega t - K_x x - K_y^{(\ell)} y\right)\right] \quad (\ell \in \mathbb{N}), \tag{19}$$

$$u_z^{\text{ref}} = \sum_{m=-\infty}^{\infty} R_m U_m(x)\ \exp\left[\mathrm{i}\left(\omega t - K_0 x\sin\theta + \kappa_y^{(m)} y\right)\right] \quad (m \in \mathbb{Z}), \tag{20}$$

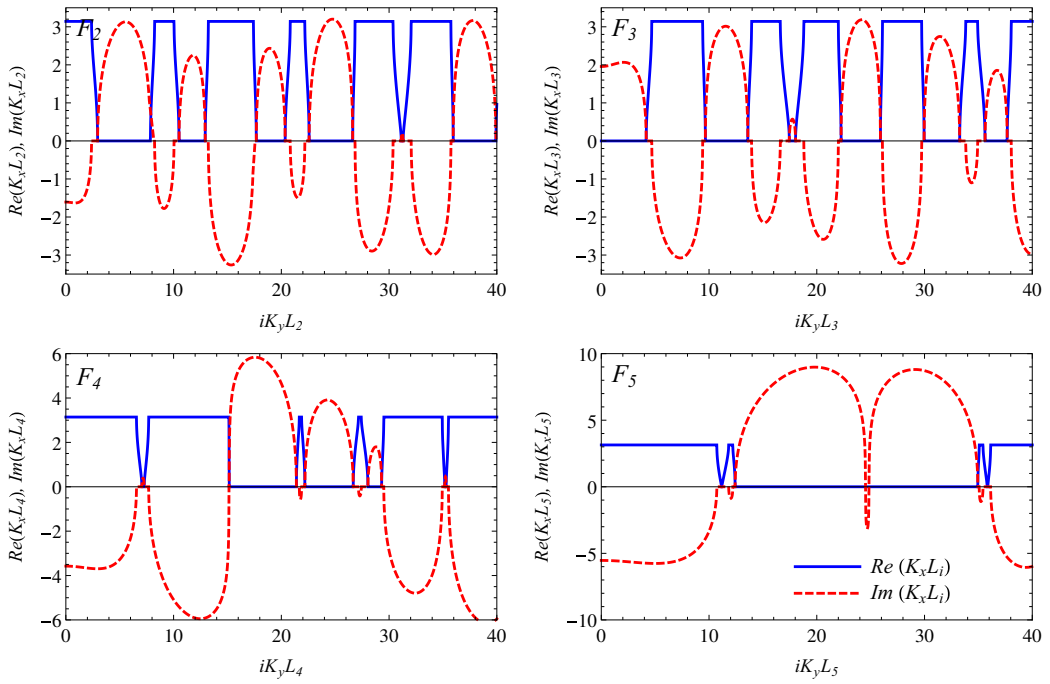

Fig. 6. Real (solid lines) and imaginary (dashed lines) parts of K_xL_i plotted against imaginary K_yL_i for Fibonacci laminates $\mathcal{F}_2$ to $\mathcal{F}_5$ at frequency $f = 220$ kHz.

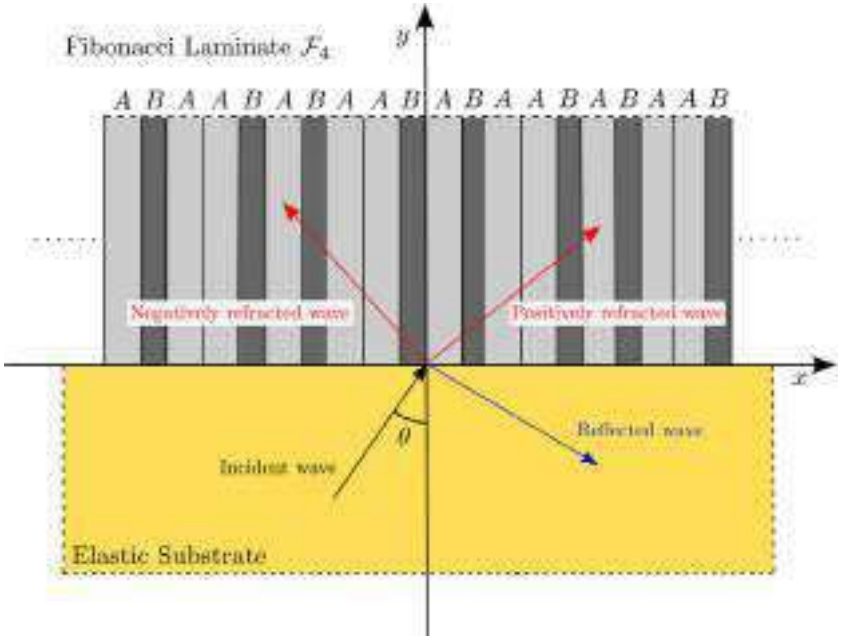

Fig. 7. Schematic of the problem of an antiplane wave approaching the interface between an elastic substrate and a Fibonacci laminate $\mathcal{F}_4$.

where $w_\ell(x)$ is the modeshape, $U_m(x) = \exp(-\mathrm{i}2m\pi x/L_i)$, $K_x = K_0 \sin\theta$ and

$$\kappa_y^{(m)} = [K_0^2 - (K_0 \sin\theta + 2m\pi/L_i)^2]^{1/2}. \tag{21}$$

According to the dispersion properties illustrated in the previous section, the real value $K_x = K_0 \sin\theta$ is associated with a finite number (N_i^f) of modes propagating along y and to an infinite number of evanescent modes along the same axis.

By imposing the continuity of displacement u_z and shear stress σ_{yz} at the interface $y = 0$, we obtain

$$\sum_{\ell=0}^{2N} \bar{T}_\ell w_\ell(x) - \sum_{m=-N}^{N} \bar{R}_m U_m(x) = 1, \tag{22}$$

$$\mu(x) \sum_{\ell=0}^{2N} K_y^{(\ell)} \bar{T}_\ell w_\ell(x) + \mu_0 \sum_{m=-N}^{N} \kappa_y^{(m)} \bar{R}_m U_m(x) = \mu_0 K_0 \cos\theta, \tag{23}$$

where $\bar{T}_\ell = T_\ell/A$ and $\bar{R}_m = R_m/A$. By applying the orthogonality conditions involving the modeshapes $w_\ell(x)$ introduced by Srivastava (2016), we can now transform (22) and (23) into a system of $2(2N+1)$ equations in $2(2N+1)$ variables, of the form

$$\begin{bmatrix} [\mathbf{Q}_1] & [\mathbf{Q}_2] \\ [\mathbf{Q}_3] & [\mathbf{Q}_4] \end{bmatrix} \{\boldsymbol{c}\} = \{\boldsymbol{d}\}, \tag{24}$$

where $\{\boldsymbol{c}\} = [\bar{T}_0, \dots, \bar{T}_{2N}, \bar{R}_{-N}, \dots, \bar{R}_N]^T$. The non-zero elements of the submatrices $[\mathbf{Q}_k]$ are given by

$$[\mathbf{Q}_1]_{pp} = \int_0^{L_i} w_p \mu w_p^* dx, \quad [\mathbf{Q}_2]_{ps} = -\int_0^{L_i} U_{s-N} \mu w_p^* dx, \tag{25}$$

$$[\mathbf{Q}_3]_{pp} = K_y^{(p)} \int_0^{L_i} w_p \mu w_p^* dx, \quad [\mathbf{Q}_4]_{ps} = \mu_0 \kappa_y^{(s-N)} \int_0^{L_i} U_{s-N} \mu w_p^* dx \tag{26}$$

($[\mathbf{Q}_1]_{ps} = [\mathbf{Q}_3]_{ps} = 0$ for $p \neq s$), where an asterisk indicates the complex conjugate and the elements of the vector $\{\boldsymbol{d}\}$ are

$$d_p = \begin{cases} \int_0^{L_i} \mu w_p^* dx \quad (p = 0, 1, \dots, 2N), \\ \mu_0 K_0 \cos\theta \int_0^{L_i} w_{p-2N-1}^* dx \quad (p = 2N+1, 2N+2, \dots). \end{cases} \tag{27}$$

The energy flux corresponding to the considered antiplane harmonic wave is given by the time averaged real part of the Poynting vector, whose components are the following

$$\mathcal{P}_x = \frac{1}{2}\mathrm{Re}\left[\omega\mu\left(K_x|\tilde{u}_z|^2 + \mathrm{i}\tilde{u}_z'\tilde{u}_z^*\right)\right], \quad \mathcal{P}_y = \frac{1}{2}\mathrm{Re}\left[\omega\mu K_y|\tilde{u}_z|^2\right], \tag{28}$$

where, considering an arbitrary transmitted mode ℓ,$\tilde{u}_z = \bar{T}_\ell w_\ell(x)$ and a dash denotes differentiation with respect to x. Willis (2016) demonstrated that $v_x^g = \partial\omega/\partial K_x = \langle\mathcal{P}_x\rangle/\langle E\rangle$ and $v_y^g = \partial\omega/\partial K_y = \langle\mathcal{P}_y\rangle/\langle E\rangle$, where E is the total energy density and $\langle\cdot\rangle$ denotes the space average performed over the elementary cell of the laminate. As a consequence, we can estimate the angle of refraction corresponding to all the considered transmitted propagating modes:

$$\theta^{\mathrm{trans}} = \arctan\left[\frac{v_x^g}{v_y^g}\right] = \arctan\left[\frac{\langle\mathcal{P}_x\rangle}{\langle\mathcal{P}_y\rangle}\right]. \tag{29}$$

By substituting expressions (28) in Eq. (29) and recalling that $\tilde{u}_z = \bar{T}_\ell w_\ell(x)$, it can be easily demonstrated that the angle of refraction associated with an arbitrary mode depends only on the modeshape $w_\ell(x)$, being not influenced by the transmission coefficient $\bar{T}_\ell$. Moreover, by observing the form of the components of the Poynting vector, it is important to note that: i.) for a positive K_y, the component $\mathcal{P}_y$ is always positive, and therefore, according to Eq. (29), a negative value of the refraction angle is certainly connected to a negative value of $\mathcal{P}_x$; ii.) the contribution to $\mathcal{P}_y$ linked to the imaginary values of K_y is zero, and consequently we do not need to account for the evanescent modes in the estimation of the angles of refraction.

3.2. Analysis of refraction, reflection and scaling

The transmission of the incoming wave at the interface of different substrate-quasicrystalline laminate pairs is now studied in detail. This section is composed of four subsections, each of which addresses a specific aspect: refracted modes (3.2.1), an analysis of modes that are reflected (3.2.2), self-similarity and scaling of the diagram collecting transition zones for a Fibonacci family of laminates (3.2.3) and the conditions to achieve the transmission of a single negatively-refracted mode (3.2.4).

3.2.1. Refracted modes

We now use Eqs. (28) and (29) to study wave refraction across the interface of different substrate–quasicrystalline laminate pairs. The wave number K_0 characterising the incident wave depends on the frequency and the properties of the substrate and is given by $K_0 = \omega\sqrt{\rho_0/\mu_0}$. Therefore, the component K_x can be evaluated through

$$K_x = K_0 \sin\theta = 2\pi f \sqrt{\frac{\rho_0}{\mu_0}} \sin\theta. \tag{30}$$

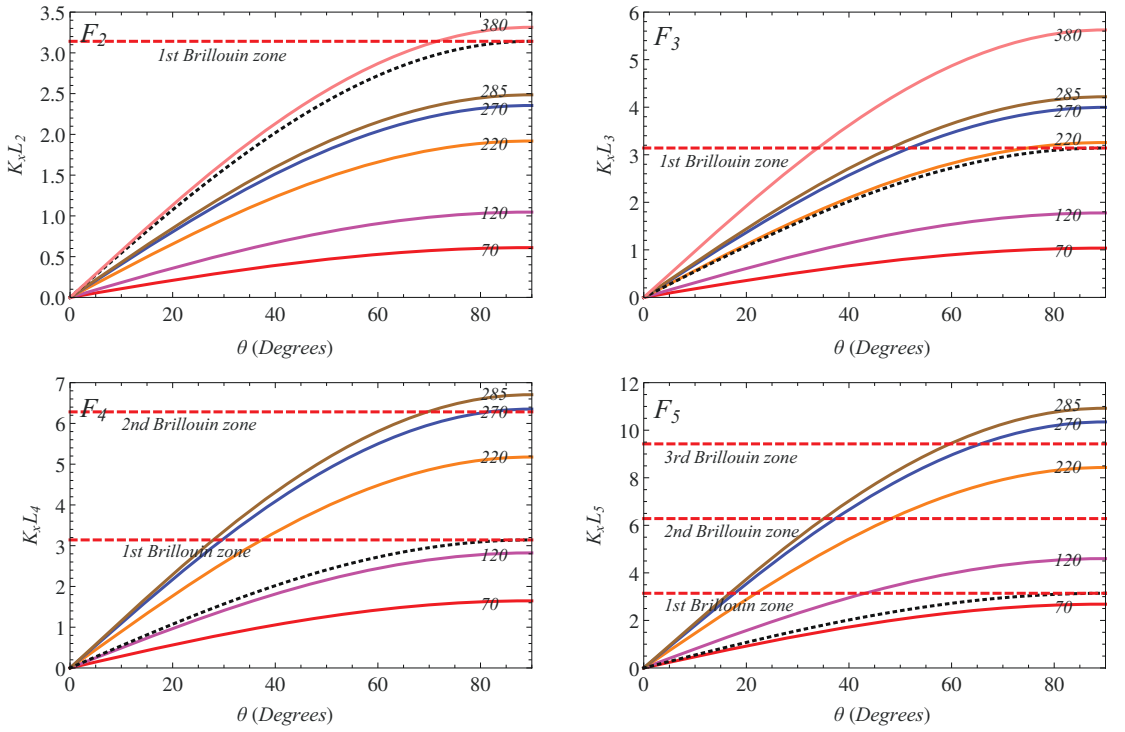

Fig. 8. Normalised wave vector component K_xL_i plotted against the angle of incidence for Fibonacci laminates $\mathcal{F}_2$ to $\mathcal{F}_5$. A substrate of aluminium has been assumed, and the horizontal dashed lines denote the limits of the different Brillouin zones. Different frequencies, whose values in kHz are reported onto the pertinent lines, are considered.

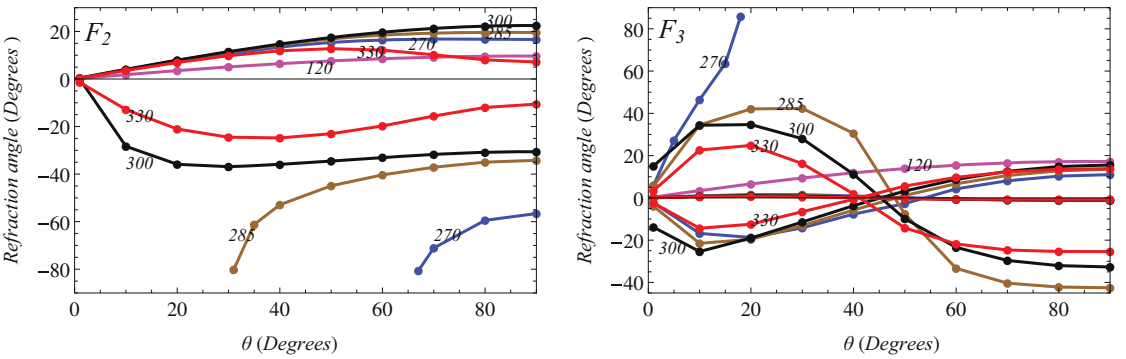

Fig. 9. Incident vs refraction angles plots for Fibonacci laminates $\mathcal{F}_2$ (left) and $\mathcal{F}_3$ (right) bonded to an aluminium substrate for five different frequencies, whose values in kHz are reported onto the pertinent lines.

By multiplying Eq. (30) to the length of an arbitrary Fibonacci cell L_i and assuming that $0 \le \theta \le \pi/2$, we deduce that the normalized wave vector of the incident wave K_xL_i belongs to the range $0 \le K_xL_i \le 2\pi f L_i \sqrt{\rho_0/\mu_0}$. For an aluminium substrate ($\rho_0 = 2700$ kg/m^3, $\mu_0 = 26$ GPa) and for four Fibonacci elementary cells ($\mathcal{F}_2$ to $\mathcal{F}_5$), K_xL_i is reported in Fig. 8 as functions of the incident angle for different values of f. The horizontal dashed lines indicate the limits of the different Brillouin zones, each spanning a range of width π along the vertical axis. We observe that as the generation index of the cell increases, the values of K_xL_i related to the same frequency increases as well. This means that for a given frequency, if we compare two laminates designed according to two different indices i, the higher order one allows access to the second (and if needed to the third) Brillouin zone for a wider range of angles of incidence.

By recalling the Floquet–Bloch analysis reported in Section 2 and the results illustrated in Figs. 3, 4 and 5, for each value of K_xL_i corresponding to a given frequency and an arbitrary angle of incidence in the interval $0 \le \theta \le \pi/2$, as for example those reported in Fig. 8, we have N_i^f real solutions of the laminate dispersion relation. *These real solutions correspond to modes propagating in the laminate, and the associated angles of refraction are plotted against* θ *in Fig. 9 for laminates* $\mathcal{F}_2$ *and* $\mathcal{F}_3$.

Several frequencies have been analysed in the calculations. For $f = 120$ kHz there is only one curve for both $\mathcal{F}_2$ and $\mathcal{F}_3$ (magenta curves) showing that only one transmitted mode is available for both layouts at this frequency. This is consistent with diagram in Fig. 11, where $f = 120$ kHz is between the first and the second transition zone for both laminates. Conversely, for both $f = 300$ and 330 kHz (black and red lines), two and three curves are detected for $\mathcal{F}_2$ and $\mathcal{F}_3$ cells, respectively (note that in the latter case one of the curves is almost coincident with the horizontal axis). In Fig. 11, the two frequencies are just after the second (third) transition zone for $\mathcal{F}_2$ ($\mathcal{F}_3$). As a consequence, the values of K_xL_2 and K_xL_3 associated with $f = 300$ and 330 kHz and with any arbitrary angle of incidence corresponds to two real values of K_yL_2 and to three real values of K_yL_3, and then to two refraction angles for $\mathcal{F}_2$ and three for $\mathcal{F}_3$.

By looking at the curves corresponding to $f = 285$, 300 and 330 kHz for laminates $\mathcal{F}_3$ in Fig. 9, we can also observe that for a certain value of the angle of incidence θ^* they change sign (positive to negative or vice versa). In this case, θ^* is the value for which $K_xL_3 = \pi$, whilst for an arbitrary $\mathcal{F}_i$ cell the angle is determined by the analogous condition $K_xL_i = \pi$. On the basis of the graphs of Fig. 8, we can deduce that for a wave with $\theta < \theta^*$, the dimensionless component of the wavenumber K_xL_i lies in the first Brillouin zone, whereas when $\theta > \theta^*$, K_xL_i belongs to the second or one of the subsequent Brillouin zones. Eq. (30) leads to the following expression

$$\theta_q^{\text{inv}} = \arcsin\left(\frac{q}{2fL_i}\sqrt{\frac{\mu_0}{\rho_0}}\right) \quad (q = 1, 2, 3, \dots). \tag{31}$$

The general formula (31) provides the critical angle of incidence θ_q^{inv} corresponding to $K_xL_i = q\pi$. For $\theta = \theta_q^{\text{inv}}$, the value of the normalised wave number K_xL_i transitions from the q-th Brillouin zone to the ensuing one, and then the refraction angle changes sign. According to this definition, the curves reported in Fig. 9 change sign at $\theta^* = \theta_1^{\text{inv}}$. By observing the curves for $f = 270$ and 285 kHz (blue and brown lines), we also note that cell $\mathcal{F}_2$ allows negative refraction only for $\theta > 65°$ and $\theta > 30°$, respectively, whereas the layout $\mathcal{F}_3$ admits the same phenomenon for any value of θ. Consequently, for these frequencies, high-order Fibonacci laminates allow negative refraction for a wider range of angles of incidence. Moreover, according to the definition introduced in Section 2.3, both $f = 270$ kHz and $f = 285$ kHz belong to a transition zone. Indeed, for $f = 270$ kHz considering the cell $\mathcal{F}_2$ we have $N_2^f = 1$ for $\theta < 65°$ and $N_2^f = 2$ for $\theta > 65°$, whereas observing the results corresponding to $\mathcal{F}_3$, it is $N_3^f = 3$ for $\theta < 20°$ and $N_3^f = 2$ for $\theta > 20°$. Consequently, $f = 270$ kHz belongs to the second transition zone for laminates $\mathcal{F}_2$ and to the third one for $\mathcal{F}_3$. Similarly, $f = 285$ kHz belongs to a transition zone (i.e. the second one) for $\mathcal{F}_2$, but it does not for $\mathcal{F}_3$: indeed, in this case for any angle of incidence, $N_3^f = 3$ (note that for both $f = 270$ kHz and $f = 285$ kHz in the case of $\mathcal{F}_3$ one of the curves in Fig. 9 is almost coincident with the horizontal axis).

3.2.2. Reflected modes

The real parts of the dimensionless wave numbers $\kappa_y^{(m)}L_i$ (different indices m are considered), corresponding to the modes reflected at the interface [see Eq. (20)], are plotted against the angles of incidence for an aluminium substrate and laminates represented by $\mathcal{F}_2$ to $\mathcal{F}_5$ in Fig. 10. Incident waves of frequencies $f = 120$ kHz and $f = 270$ kHz are assumed for the calculations. According to the representation of the reflected wave field (20), each one of these real parts is associated with a reflected mode propagating in the substrate, whereas if $\kappa_y^{(m)}L_i$ is imaginary the corresponding waves are evanescent. We can observe that for a fixed value of the incident wave frequency, the number of propagating reflected modes increases at increasing order of the cell. Alternatively, at a given elementary cell $\mathcal{F}_i$, a higher number of propagating reflected modes for higher incident frequencies is found. By looking at the curves, we note that for any Fibonacci cell and any value of the frequency there exists at least one propagating mode, corresponding to $m = 0$. This can be easily explained by recalling Eq. (21) and specialising it to $m = 0$. This leads to $\kappa_y^{(0)}L_i = K_0L_i\cos\theta = 2\pi L_i\sqrt{\rho_0/\mu_0}\cos\theta$. As a consequence, in order to have *reflectionless* negative refraction using a Fibonacci laminate, it is always required that the amplitude R_0 of the mode $m = 0$ vanishes for some ranges of incident frequencies or incident angles. This is a sufficient condition in the cases where the only propagating reflected wave is that associated with $m = 0$, which occurs if

$$0 < fL_i\sqrt{\frac{\rho_0}{\mu_0}}(1 - \sin\theta) < 1. \tag{32}$$

Conversely, if we have $fL_i\sqrt{\rho_0/\mu_0}(1 - \sin\theta) \geq 1$, as for cases of laminates $\mathcal{F}_3$, $\mathcal{F}_4$ and $\mathcal{F}_5$ reported in Fig. 10, several additional reflected waves can propagate in the substrate, and then in order to obtain reflectionless wave propagation it is required that the amplitudes of all these modes are zero, i.e. $R_m = 0$. Furthermore, also in cases where the reflectionless conditions are verified, the real consistency of the evaluated reflected and transmitted fields should be checked through the balance of the energy flow at the interface, following the procedure proposed by Srivastava (2016) and Willis (2016). The cases analysed further in the paper do not encompass reflectionless phenomena.

3.2.3. Self-similarity and scaling of the transition zone layout

The arrangement of the transition zones, that are sketched in red, for laminates designed according to cells $\mathcal{F}_2$ to $\mathcal{F}_6$ is reported in Fig. 11 as a function of the frequency. The number written on each complementary grey range of frequencies denotes the number of propagating modes N_i^f that is constant in the interval. When coupled to the substrate, each of these propagating modes has a different angle of refraction.

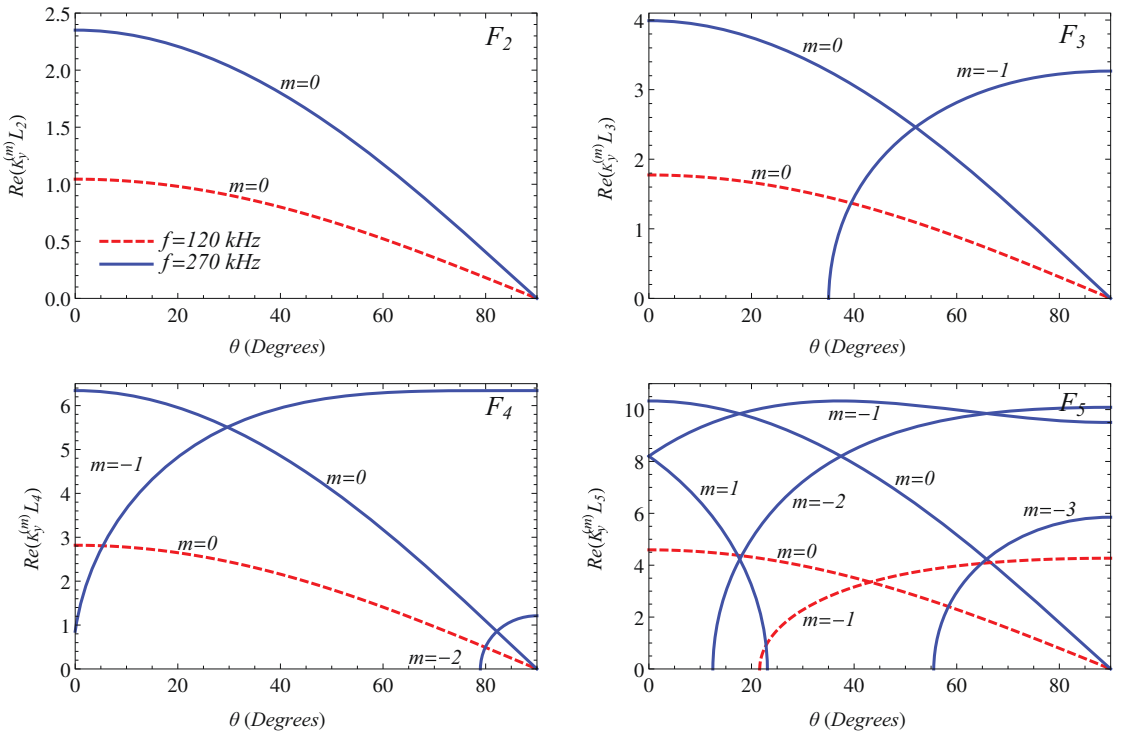

Fig. 10. Real part of the normalised wave vector component $\kappa_y^{(m)}L_i$, corresponding to the modes reflected at the interface, plotted against the angle of incidence for Fibonacci laminates $\mathcal{F}_2$ to $\mathcal{F}_5$ for frequencies $f = 120$ kHz (dashed lines) and $f = 270$ kHz (solid lines) of the incident wave. A substrate of aluminium has been considered.

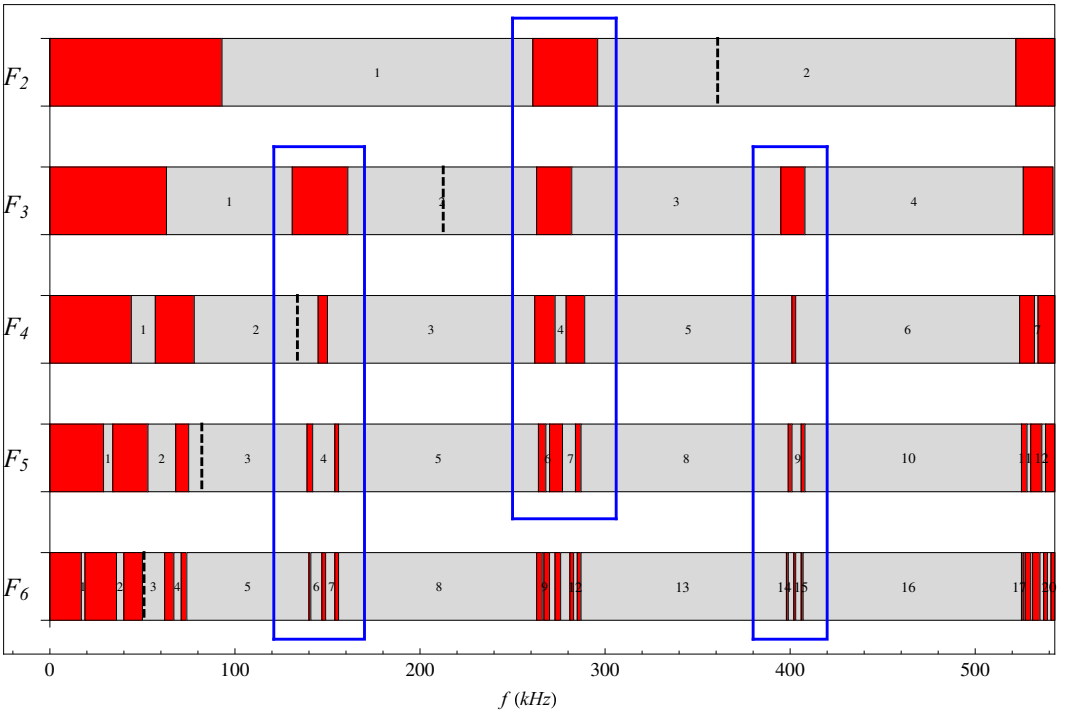

Fig. 11. Diagram reporting, in the grey zones, the number N_i^f of real solutions K_y of the dispersion relation for cells $\mathcal{F}_2$ to $\mathcal{F}_6$ as a function of the frequency. Transition zones are highlighted in red. Blue rectangles contain transition zones affected by local scaling. The covered range of frequencies ($0 \le f \le 543$ kHz) corresponds to the pseudo-period of the Kohmoto's invariant $I_0(2\pi f)$. For each cell, the black, dashed vertical line marks the minimum frequency to have a transmitted wave in the second Brillouin zone. (For interpretation of the references to colour in this figure legend, the reader is referred to the web version of this article.)

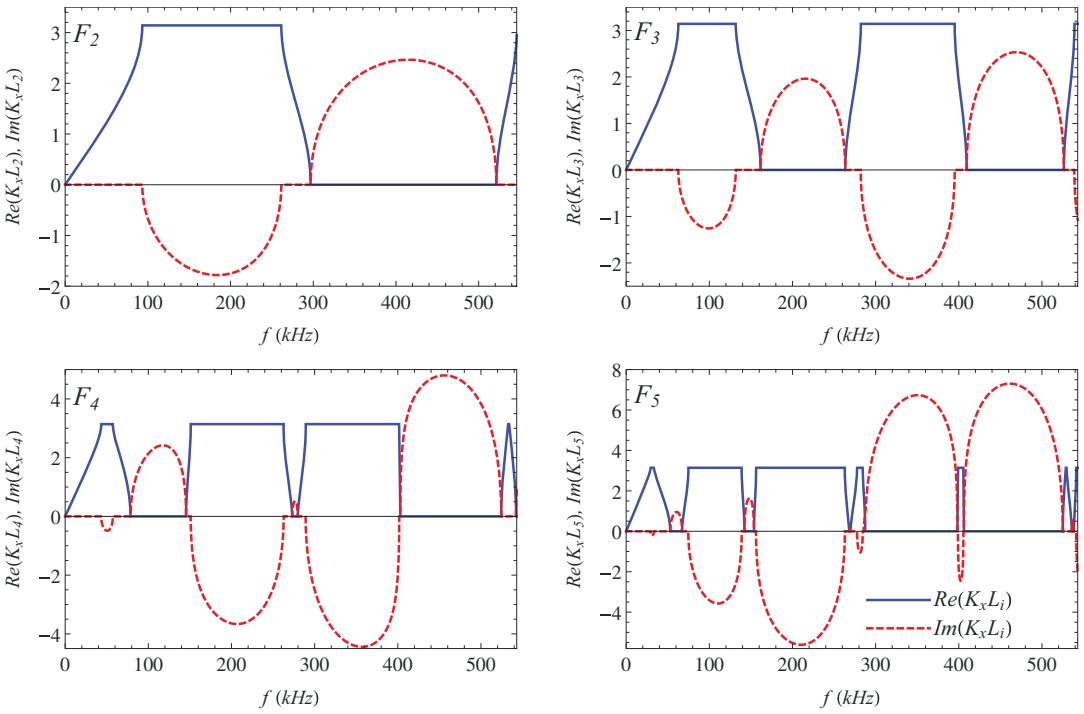

Fig. 12. Real (solid lines) and imaginary (dashed lines) parts of K_xL_i plotted against the frequency f for Fibonacci laminates $\mathcal{F}_2$ to $\mathcal{F}_5$ by assuming $K_y = 0$.

Let us observe the sets of transition zones enclosed by blue rectangles in Fig. 11. It is easy to note that, starting from the top, they are all composed of a single large transition zone followed by a thinner one almost centered at the same value of the frequency. Then, a pair and sets of three and five zones come next in order. The pattern is typically self similar and analogous to that highlighted by Gei (2010) and Morini and Gei (2018) for quasicrystalline-generated structural waveguides. Self similarity is governed by a local scaling whose factor can be obtained by analysing the specialised Kohmoto's invariant $I_0(\omega)$ (13) overseeing transverse wave propagation in the laminate (i.e. $K_y = 0$). As discussed in Section 2.2, in this case the transfer matrix (7) and dispersion relation (10) assume a form similar to that derived by Morini and Gei (2018) with traces t_i following the recursive relation (11). Consequently, for $K_y = 0$ the dispersion curves reported in Fig. 12 for laminates $\mathcal{F}_2$ to $\mathcal{F}_5$ and the associated stop/pass band distribution possess the same features of those obtained in (Morini and Gei, 2018). In the same figure, by assuming $K_y = 0$, the real and imaginary parts of K_xL_i are sketched against the frequency for the interval $0 \le f \le 543$ kHz that corresponds to the pseudo-period of function $I_0(2\pi f)$. The layout of the dispersion curves reveals that for any cell $\mathcal{F}_i$ the position of pass bands coincide with that of transition zones reported in Fig. 11.

Eqs. (16) and (17) can be employed to analyse the scaling occurring within some frequency ranges of the stop/pass band layout associated with the dispersion curves reported in Fig. 12, and then in the transition zone diagram of Fig. 11. As an example, let us consider the seventh transition zone in the plot for $\mathcal{F}_5$ in Fig. 11. We can easily note that it coincides with the seventh pass band $\{f_5^B - f_5^A\}$ of $\mathcal{F}_5$ centred at $f^* = 273.25$ kHz in Fig. 12. Numerical calculations yield $f_5^B - f_5^A = 7.50$ kHz and $\lambda = 4.80$. By using the relationship (17), we finally get $f_2^B - f_2^A \approx (f_5^B - f_5^A)\lambda = 35.99$ kHz, which is in very good agreement with the value provided by the actual computations (i.e. $f_2^B - f_2^A = 35.91$ kHz). The same scaling behaviour is detected by comparing the seventh and fifteenth transition zones of $\mathcal{F}_6$, centred at $f^* = 148.27$ kHz and $f^* = 402.32$ kHz, respectively, to the second and fourth of $\mathcal{F}_3$, respectively. In the former case, $\lambda = 28.18$, the actual range $f_3^B - f_3^A$ measures 28.81 kHz whereas the scaling provides $f_3^B - f_3^A \approx (f_6^B - f_6^A)\lambda = 28.75$ kHz; in the latter, $\lambda = 136.61$, scaling predicts $f_3^B - f_3^A \approx (f_6^B - f_6^A)\lambda = 14.34$ kHz whereas on the diagram, $f_3^B - f_3^A = 14.36$ kHz. Both comparisons are very accurate.

A second type of scaling, called *global* scaling in Morini and Gei (2018), exhibits in the diagram of Fig. 11. For a reason that will be clarified in the next subsection, we consider the range of frequencies from zero to the upper boundary of the second transition zone and denote by $\Delta_g f_i$ this interval for the sequence $\mathcal{F}_i$. In an approximate way, the global scaling makes the connection between $\Delta_g f_i$ and $\Delta_g f_{i+3}$ ($\Delta_g f_{i+6}$) as $\Delta_g f_i \approx \bar{\lambda}\Delta_g f_{i+3}$ ($\Delta_g f_i \approx \bar{\kappa}\Delta_g f_{i+6}$) where $\bar{\lambda}$ ($\bar{\kappa}$) is the average of parameter λ (κ) on $\Delta_g f_{i+3}$ ($\Delta_g f_{i+6}$) and is based on the similar behaviour of trace $t_i(\omega)$ with $t_{i+3}(\bar{\lambda}\,\omega)$ ($t_{i+6}(\bar{\kappa}\,\omega)$), the latter with a scaled argument. As an example, in the plot of Fig. 11, $\Delta_g f_3 = 162$ kHz and $\Delta_g f_6 = 36$ kHz, so that their ratio is equal to 4.50, whereas $\bar{\lambda}$ turns out to be $\bar{\lambda} = 4.46$. Moreover, as $\Delta_g f_2 = 297$ kHz and $\Delta_g f_8 = 14.8$ kHz, their ratio is equal to 20.07 that must be compared with $\bar{\lambda} = 18.05$.

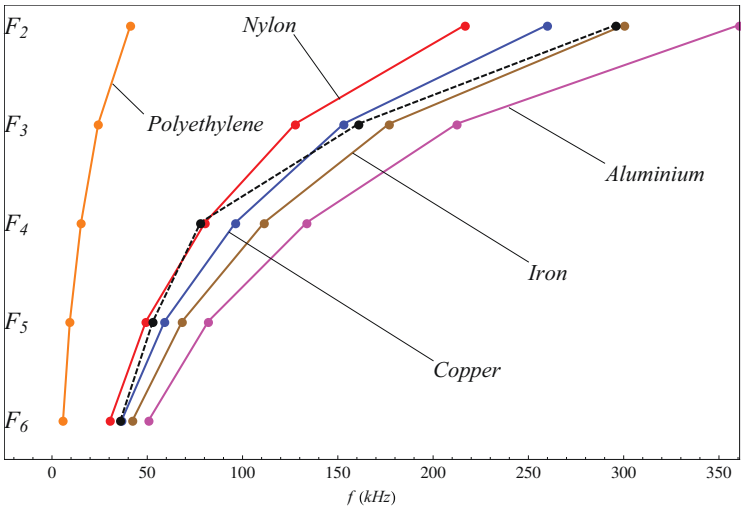

Fig. 13. Plot of the minimum frequency $f_i^{\min}$ (solid lines) to gain access to the second Brillouin zone for different substrate-laminate systems (properties of phases *A* and *B* of the laminates, made up of PMMA and steel, are the same for all cases). Different substrates are assumed: aluminium (magenta line), iron (brown line), copper (blue line), nylon (red line) and polyethylene (orange line). Black points connected by the black dashed line represent the values of the frequency associated with the upper limit of the second transition zone ($\tilde{f}_i$) for the corresponding laminate. (For interpretation of the references to colour in this figure legend, the reader is referred to the web version of this article.)

It is important to remark that the scaling analyses here reported are restricted to the laminate whose phases (i.e. PMMA and steel) match those employed by Nemat-Nasser (2015a); Srivastava (2016); Willis (2016) and that, as suggested by Morini and Gei (2018), the ranges of frequencies where the two scalings are meaningful may change significantly depending on the properties of the two components of the composite. An interesting application to explore in a future study is the case of *canonical* Fibonacci laminates[2], for which at some well-defined frequencies (i.e. the *canonical* frequencies) the trajectories on the Kohmoto's surface correspond to the closed orbits pinpointed by the six saddle points and then the local scaling is therein more accurate.

3.2.4. Transmission of a single negatively-refracted mode

In the diagram reported in Fig. 11, for each $\mathcal{F}_i$, the black dashed line marks the minimum frequency required to have at least one value of the dimensionless wave vector component K_xL_i in the second Brillouin zone for the laminate-substrate pair studied so far (PMMA-steel laminate bonded to an aluminium substrate). These values, indicated henceforth as $f_i^{\min}$, correspond exactly to the short-dashed black curves reported in Fig. 8 that approach the second Brillouin zone ($K_xL_i = \pi$) for $\theta = \pi/2$, leading, through Eq. (30), to $f_i^{\min} = \sqrt{\mu_0}/(2L_i\sqrt{\rho_0})$.

The possibility of having a real K_xL_i in the second Brillouin zone at the interface is crucial in order to induce only a single negatively-refracted wave in the laminate. Indeed, the data reported in Fig. 9 (left) for $\mathcal{F}_2$ show that if K_xL_i evaluated using expression (30) is limited to the first Brillouin zone, the transmitted propagating pattern consists of either a positively refracted mode or a pair of positively and negatively-refracted waves. In order to have only one mode propagating in the laminate with a negative refraction angle, we need to set up a value for K_xL_i in the second Brillouin zone and, at the same time, to select an elastic substrate for which $f_i^{\min} < \tilde{f}_i$, where $\tilde{f}_i$ is the highest frequency of the second transition zone. This additional condition is due to the fact that for $f < \tilde{f}_i$ just one transmitted mode –or at least one– is available for some values of K_xL_i and two for the remaining values. As a consequence, a Fibonacci laminate $\mathcal{F}_i$ can transmit a single negatively-refracted mode should the frequency of the incident wave belongs to the interval $f_i^{\min} \le f \le \tilde{f}_i$.

By observing Fig. 11, we can easily note that frequencies $f_i^{\min}$ marked by the dashed line are larger than $\tilde{f}_i$ for all the layouts considered until now. Therefore, the condition $f_i^{\min} \le f \le \tilde{f}_i$ is not met: the aluminium substrate cannot be used for this purpose.

In Fig. 13, the values of $f_i^{\min}$ associated with different substrates are compared with those of $\tilde{f}_i$ for laminates up to $\mathcal{F}_6$ composed of the same phases (PMMA and steel) as above. In addition to aluminium, iron ($\rho_0 = 7860$ kg/m^3, $\mu_0 = 52.5$ GPa), copper ($\rho_0 = 8940$ kg/m^3, $\mu_0 = 44.7$ GPa), nylon ($\rho_0 = 1150$ kg/m^3, $\mu_0 = 4$ GPa) and polyethylene ($\rho_0 = 930$ kg/m^3, $\mu_0 = 0.117$ GPa) substrates are considered. We note that also for iron $f_i^{\min} > \tilde{f}_i$, therefore a wave travelling in this material cannot be converted in a single negatively-refracted mode by means of the quasicrystalline laminates under investigation. Conversely, relative soft substrates such as polyethylene and nylon are associated with values of $f_i^{\min}$ such that $f_i^{\min} < \tilde{f}_i$, and

[2] The properties of the two phases *A* and *B* in order to assemble a *canonical* Fibonacci laminate can be inferred from the analogous study on 1-D quasicrystalline waveguides performed by Morini and Gei (2018).

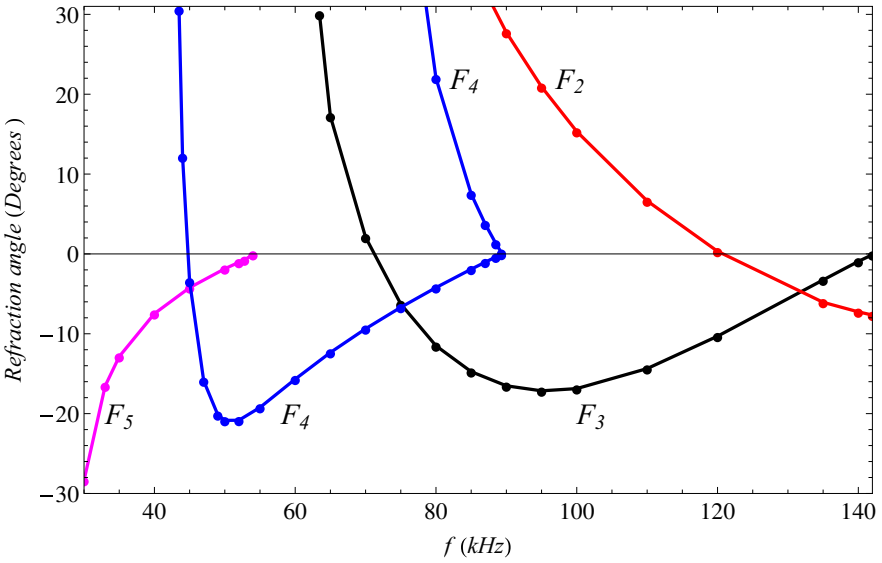

Fig. 14. Angles of refraction corresponding to an incident angle $\theta = 20^\circ$ plotted versus the frequency for Fibonacci laminates $\mathcal{F}_2$ to $\mathcal{F}_5$. A polyethylene substrate ($\rho_0 = 930$ kg/m^3, $\mu_0 = 0.117$ GPa) has been assumed. Curves for $\mathcal{F}_4$ and $\mathcal{F}_5$ are interrupted when approaching the horizontal line as this corresponds to the condition $K_x L_4 = K_x L_5 = 2\pi$ for which the values of $K_x L_4$ and $K_x L_5$ leave the second Brillouin zone and enter the third. $\mathcal{F}_2$ coincides with the case studied by Srivastava (2016).

then waves with $f_i^{\min} \le f \le \tilde{f}_i$ propagating in these media can be potentially converted in one single mode with negative refraction angle using the laminates at hand.

It becomes clear now that the global scaling studied in the previous subsection can be a useful tool to predict for which quasicrystalline laminate $\mathcal{F}_i$ (when coupled to a given elastic substrate) the condition $f_i^{\min} < \tilde{f}_i$ is met, assuring one single negative refracted mode.

The angles of refraction corresponding to propagating modes transmitted at the interface between a polyethylene substrate and a PMMA-steel composite are reported as functions of the frequency in Fig. 14 where we have assumed the constant value $\theta = 20^\circ$. The curves for $\mathcal{F}_4$ and $\mathcal{F}_5$ are interrupted approaching the horizontal axis as, with the increase of the frequency, this corresponds to $K_x L_4 = K_x L_5 = 2\pi$. At this value, both $K_x L_4$ and $K_x L_5$ leave the second Brillouin zone and enter the third. This plot again shows that high-order Fibonacci cells admit transmission of one single negatively-refracted mode at relatively low frequencies in contrast to the a laminate $\mathcal{F}_2$ (as studied by Srivastava (2016); Willis (2016) and Srivastava and Willis (2017)) that admits the same phenomenon only for $f > 120$ kHz. This means that, considering the same angle of incidence, high order quasicrystalline laminates yield single negatively-refracted modes at lower frequencies with respect to standard two-phase periodic laminates. More precisely, by considering an arbitrary angle of incidence θ, and assuming that the condition $f_i^{\min} \le f \le \tilde{f}_i$ is satisfied, a laminate $\mathcal{F}_i$ can provide a single negatively-refracted mode for waves whose frequencies belong to the range

$$\sqrt{\frac{\mu_0}{\rho_0}}\frac{1}{2L_i \sin\theta} < f < \sqrt{\frac{\mu_0}{\rho_0}}\frac{1}{L_i \sin\theta}. \tag{33}$$

The condition (33) can be easily derived through Eq. (30). Accordingly, if we have $f > \sqrt{\mu_0/\rho_0}/(L_i \sin\theta)$, then $K_x L_i > 2\pi$, and the normalized wave vector switches from the second to the third Brillouin zone, and the refraction angle changes sign becoming positive. Similarly, an incident wave with frequency $f_i^{\min} \le f \le \tilde{f}_i$ and satisfying the condition (33) can be converted into a single negatively-refracted mode if the angle of incidence lays in the interval $\theta_1^{\text{inv}} < \theta < \theta_2^{\text{inv}}$, where θ_1^{inv} and θ_2^{inv} are given by the general relation (31), yielding

$$\arcsin\left(\frac{1}{2fL_i}\sqrt{\frac{\mu_0}{\rho_0}}\right) < \theta < \arcsin\left(\frac{1}{fL_i}\sqrt{\frac{\mu_0}{\rho_0}}\right). \tag{34}$$

In agreement to what we have observed in Fig. 9, for $\theta > \arcsin\left(\sqrt{\frac{\mu_0}{\rho_0}}/(fL_i)\right)$ the dimensionless wave vector component $K_x L_i$ enters the third Brillouin zone, and then the corresponding refraction angle goes from negative to positive.

Plots of the refracted displacement amplitude field $u_z^{\text{trans}}(x, y)$, Eq. (19), for a representative case of the coupling between the laminate and a polyethylene substrate are sketched in Fig. 15. In this figure, the wavefronts related to a 100 kHz signal approaching, with an angle $\theta = 20^\circ$, the interface between a polyethylene substrate and Fibonacci laminates $\mathcal{F}_2$ and $\mathcal{F}_3$ are reported. Only one transmitted mode is available in both systems (see Fig. 14, $f = 100$ kHz). We can recognise the negative

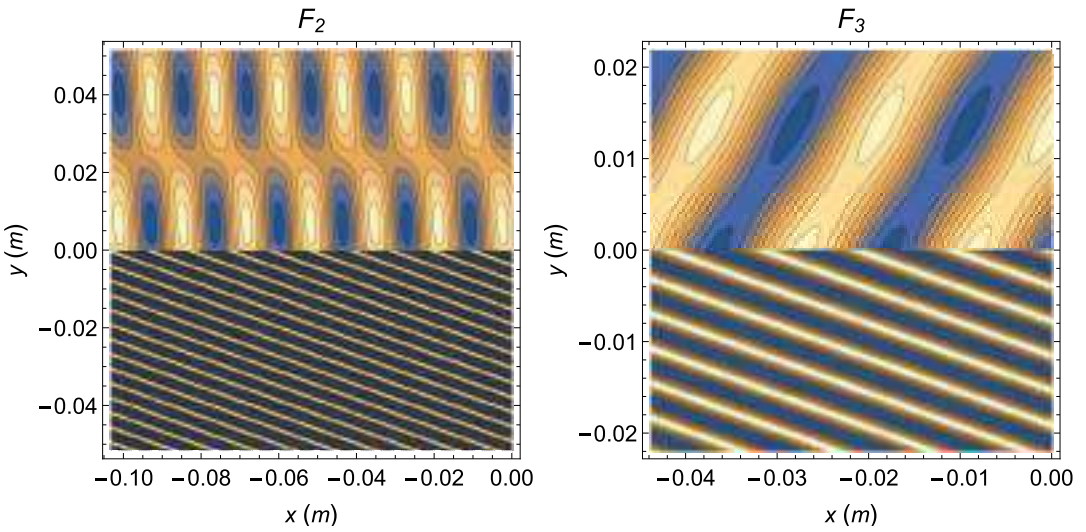

Fig. 15. Two-dimensional contour plots illustrating the displacement amplitude of the refracted wave $u_z^{\text{trans}}(x, y)$, Eq. (19), of an antiplane signal of frequency $f = 100$ kHz and incident angle $\theta = 20^\circ$ at the interface between a polyethylene substrate and laminates $\mathcal{F}_2$ (left) and $\mathcal{F}_3$ (right). Negative refraction is achieved on the right-hand panel.

refraction for the wave propagating in cell $\mathcal{F}_3$, whereas for $\mathcal{F}_2$ a positive one is obtained. It is worth to remark that the studied angle of refraction θ^{trans} does not correspond, however, to that formed by the normal to the average refracted wavefront as the former traces the direction of the energy flux (see also Nemat-Nasser (2015a)). In the reported case, the use of both Poynting vector and group velocity components provide, through Eq. (29), $\theta^{\text{trans}} = 15.33^\circ$ and $\theta^{\text{trans}} = -16.87^\circ$, respectively for the left and right-hand side of the figure, in agreement with the data reported in Fig. 14.

4. Conclusions

Fibonacci laminates are a family of two-phase multilayered composites whose layouts, each associated with an integer index, are generated following the Fibonacci substitution rule. They are a subset of the more general class of quasicrystalline laminates. The main goal of the article is to address the problem of negative refraction of antiplane shear waves transmitted at an interface between an elastic substrate hosting the incoming signal and one of those laminates, arranged such that the layering direction is orthogonal to the interface.

To achieve the objective, in the first part, a dispersion analysis for Fibonacci laminates is carried out adopting the classical Floquet–Bloch technique. In particular, number and properties of propagating modes are revealed for each layout at varying frequency. A key property of the dispersion diagrams is the occurrence of particular ranges of frequencies, called transition zones, where the number of propagating modes depends on the frequency itself.

In the second part of the paper, transmission of antiplane waves across the substrate-laminate interface is addressed by applying the normal mode decomposition technique to couple the response of the composite to the properties of the substrate. The angle of refraction is estimated through the evaluation of the Poynting vector. The conclusions can be summarised as follows:

– with respect to the classical bilayer, Fibonacci laminates can transmit negatively-refracted waves for a wider range of angles of incidence, with a trend that increases monotonically at increasing index; in some cases, negative refraction is attainable for any angle of incidence;

– by assuming the same angle of incidence for the impinging wave, using the proposed quasicrystalline composite it is possible to produce a single transmitted negatively-refracted wave at lower frequencies without the need to change the materials composing the laminae as required for a simple bilayer. This is achievable as propagating modes in the second Brillouin zone become available at lower frequencies. The ranges of frequencies and incidence angles at which this property can be achieved are reported and discussed in detail;

– the global scaling studied by exploiting the properties of the Kohmoto's invariant may be used as a predicting tool to select the most suitable laminate of the family that, in combination to a given substrate, may assure the availability of a single negatively-refracted transmitted mode.

The outcomes of this research, though restricted to a particular combination of the materials of the two phases, indicate that quasicrystalline laminates may broaden the possibilities of using multilayers as building blocks for the construction of metamaterials able to transmit negatively-refracted waves.

Acknowledgments

L.M. and M.G. acknowledge funding from the EU Horizon 2020 research and innovation programme under Marie Skłodowska–Curie Actions COFUND grant SIRCIW, agreement no 663830.

References

Brun, M., Guenneau, S., Movchan, A.B., Bigoni, D., 2010. Dynamics of structural interfaces: filtering and focussing effects for elastic waves. J. Mech. Phys. Solids 58, 1212–1224.
Chen, Y.Y., Hu, G.K., Huang, G.L., 2017. A hybrid elastic metamaterial with negative mass density and tunable bending stiffness. J. Mech. Phys. Solids 105, 179–198.
Gei, M., 2010. Wave propagation in quasiperiodic structures, stop/pass band distribution and prestress effects. Int. J. Solids Struct. 47, 3067–3075.
Guenneau, S., Movchan, A.B., Petursson, G., Ramakrishna, S.A., 2007. Acoustic metamaterials for sound focusing and confinement. New J. Phys. 9, 399.
Hegemier, G., Nayfeh, A.H., 1973. A continuum theory for wave propagation in laminated composites–case 1: propagation normal to the laminates. J. Appl. Mech. 40, 503–510.
Hussein, M.I., Leamy, M., Ruzzene, M., 2014. Dynamics of phononic materials and structures: historical origins, recent progress, and future outlook. Appl. Mech. Rev. 66, 040802.
Jones, I.S., Movchan, A.B., Gei, M., 2011. Waves and damage in structured solids with multi-scale resonators. Proc. R. Soc. A 467, 964–984.
Khelif, A., Deymier, P.A., Djafari-Rouhani, B., Vasseur, J.O., Dobrzynski, L., 2003. Two-dimensional phononic crystal with tunable narrow pass band: application to a waveguide with selective frequency. J. Appl. Phys. 93, 1308–1311.
Kolar, M., Ali, M.K., 1989. Generalized fibonacci superlattices, dynamical trace maps, and magnetic excitations. Phys. Rev. B 39, 426–432.
Kolar, M., Nori, F., 1990. Trace maps of general substitutional sequences. Phys. Rev. B 42, 1062–1065.
Lee, J.-H., Singer, J.P., Thomas, E.L., 2012. Micro-/nanostructured mechanical metamaterials. Adv. Mater 24, 4782–4810.
Morini, L., Gei, M., 2018. Waves in one-dimensional quasicrystalline structures: dynamical trace mapping, scaling and self-similarity of the spectrum. J. Mech. Phys. Solids 119, 83–103.
Morvan, B., Tinel, B., Hladky-Hennion, A.-C., Vasseur, J., Dubus, B., 2010. Experimental demonstration of the negative refraction of a transverse elastic wave in a two-dimensional solid phononic crystal. Appl. Phys. Lett. 96, 101905.
Nemat-Nasser, S., 1972. Harmonic waves in layered composites. J. Appl. Mech. 39, 850–852.
Nemat-Nasser, S., 2015. Anti-plane shear waves in periodic elastic composites: band structure and anomalous wave refraction. Proc. R. Soc. A 471, 20150152.
Nemat-Nasser, S., 2015. Refraction characteristics of phononic crystals. Acta Mech. Sin. 31, 481–493.
Nemat-Nasser, S., Fu, F., Minagawa, S., 1975. Harmonic waves in one-,two- and three-dimensional composites: bounds for eigenfrequencies. Int. J. Solids Struct. 11, 617–642.
Pennec, Y., Vasseur, J.O., Djafari-Rouhani, B., Dobrzyski, L., Deymier, P.A., 2010. Two-dimensional phononic crystals: examples and applications. Surf. Sci. Rep. 65, 229–291.
Poddubny, A.N., Ivchenko, E.L., 2010. Photonic quasicrystalline and aperiodic structures. Physica E 43, 1871–1895.
Roberts, R., Achenbach, J.D., Ko, R., Adler, L., Jungman, A., Quentin, G., 1983. Beam splitting at the reflection of elastic waves by a periodic surface profile. J. Acoustic Soc. America 74, 1638–1640.
Roberts, R., Achenbach, J.D., Ko, R., Adler, L., Jungman, A., Quentin, G., 1985. Reflection of a beam of elastic waves by a periodic surface profile. Wave Motion 7, 67–77.
Romanoni, M., Gonella, S., Apetre, N., Ruzzene, M., 2009. Two-dimensional periodic actuators for frequency-based beam steering. Smart Mat. Struct. 18, 125023.
Rudykh, S., Boyce, M.C., 2014. Transforming wave propagation in layered media via instability-induced interfacial wrinkling. Phys. Rev. Lett. 112, 034301.
Shmuel, G., Band, R., 2016. Universality of the frequency spectrum of laminates. J. Mech. Phys. Solids 92, 127–136.
Srivastava, A., 2015. Elastic metamaterials and dynamic homogenization: a review. Int. J. Smart Nanomater. 6, 41–60.
Srivastava, A., 2016. Metamaterial properties of periodic laminates. J. Mech. Phys. Solids 96, 252–263.
Srivastava, A., Willis, J.R., 2017. Evanescent wave boundary layers in metamaterials and sidestepping them through a variational approach. Proc. R. Soc. A 473. 20160765
Sukhovich, A., Jing, L., Page, J.H., 2008. Negative refraction and focussing of ultrasound in two-dimensional phononic crystals. Phys. Rev. B 77, 014301.
Sun, C.-T., Achenbach, J., Herrmann, G., 1968. Time-harmonic waves in a stratified medium propagating in the direction of the layering. J. Appl. Mech. 35, 408–411.
Thomson, W., 1950. Transmission of elastic waves in stratified solid medium. J. Appl. Physics 21, 89–94.
Vines, R.E., Wolfe, J.P., Every, A.V., 1999. Scanning phononic lattices with ultrasound. Phys. Rev. B 60, 11871–11874.
Wang, G., Yu, D., Wen, J., Liu, Y., Wen, X., 2004. One-dimensional phononic crystals with locally resonant structures. Phys. Lett. A 327, 512–521.
Willis, J.R., 2016. Negative refraction in a laminate. J. Mech. Phys. Solids 97, 10–18.
Wu, L.-Y., Wu, M.-L., Chen, L.-W., 2009. The narrow pass band filter of tunable 1D phononic crystals with a dielectric elastomer layer. Smart Mat. Struct. 18, 015011.
Yang, S., Page, J.H., Liu, Z., Cowan, M.L., Chan, C.T., Sheng, P., 2004. Focusing of sound in a 3D phononic crystal. Phys. Rev. Lett. 93, 024301.
Zhang, X., Liu, Z., 2004. Negative refraction of acoustic waves in two-dimensional phononic crystals. Appl. Phys. Lett. 85, 341–342.
Zhu, R., Liu, X.N., Hu, G.K., Sun, C.T., Huang, G.L., 2014. Negative refraction of elastic waves at the deep-subwavelength scale in a single-phase metamaterial. Nature Comm. 5, 5510.